Earth Planet. Sci. Lett. 691 (2026) 120223

Contents lists available at ScienceDirect

Earth and Planetary Science Letters

journal homepage: www.elsevier.com/locate/epsl

Crustal anisotropic velocity structure beneath California constrained by *P* and *PmP* traveltimes: Implications for fluid-promoted creeping along the central San Andreas Fault

Jing Chen [a], Tianjue Li [a], Xiao Xiao [a], Shucheng Wu [b], Yiming Bai [a], Guoxu Chen [c], Bingfeng Zhang [a], Mijian Xu [d], Ping Tong [a,e,*]

[a] School of Physical and Mathematical Sciences, Nanyang Technological University, Singapore, 637371, Singapore
[b] State Key Laboratory of Geological Processes and Mineral Resources, China University of Geosciences, Wuhan, China
[c] Department of Civil and Environmental Engineering, The Hong Kong Polytechnic University, Hong Kong SAR, China
[d] Department of Physics, University of Toronto, Toronto, Canada
[e] Earth Observatory of Singapore, Nanyang Technological University, Singapore, 639798, Singapore

ARTICLE INFO

Editor: Dr H Thybo

Keywords:
Seismic tomography
Seismic anisotropy
San Andreas Fault
Fault creep
Reflection traveltimes
Fluid infiltration

ABSTRACT

Fault creep plays a critical role in the earthquake cycle and seismic hazard estimation, yet its controlling mechanisms along the central San Andreas Fault remain debated. Using >40 years of *P* and *PmP* traveltime data, we image crustal velocity heterogeneity and azimuthal anisotropy across California. The inclusion of *PmP* data significantly improves illumination of the middle-to-lower crust, revealing that fluids may promote the central San Andreas Fault (SAF) creep primarily by forming frictionally weak materials. Specifically, aqueous fluids are imaged as low-velocity anomalies beneath the creeping segment, with fluid volume nearly proportional to the fault creep rate. However, low-velocity anomalies, identified as partial melting, are also revealed beneath the locked Loma Prieta segment to the north. This comparison suggests that elevated pore pressure, arising from either aqueous fluids or melts, may not be the primary driver of creep. Instead, aqueous fluids promote the formation of frictionally weak minerals that facilitate creep. In addition, fault-parallel fast velocity directions along the creeping segment further support the presence of frictionally weak minerals and their role in facilitating fault creep. This anisotropic pattern terminates at the locked Loma Prieta segment possibly due to enhanced normal stress. Our detailed crustal anisotropic velocity model offers new insights into the mechanisms governing fault creep, with potential applicability to major fault systems worldwide.

1. Introduction

Fault creep is an aseismic fault slip behavior that accommodates lithospheric deformation by slow slip without generating high-frequency seismic waves (Bürgmann, 2018). It contrasts with seismic fault slip associated with stick-slip failure of asperities (McLaskey and Glaser, 2011), such as large damaging earthquakes and small repeating earthquakes (Uchida and Bürgmann, 2019). Fault creep is commonly thought to accommodate a portion of the fault slip budget aseismically, thereby reducing the likelihood of nucleating large earthquakes (Bürgmann, 2018). For example, in California, creep along the central San Andreas Fault (SAF) was first recognized near Hollister in 1960 (Steinbrugge et al., 1960). Subsequent studies identified fault creep along a 175-km-long segment from San Juan Bautista to Cholame (Jolivet et al., 2015; Titus et al., 2006), bounded by the Loma Prieta segment to the northwest and the Carrizo segment to the southeast (Fig. 1). Due to the creeping behavior, no historical earthquakes with magnitude exceeding 7.0 have occurred over the past 1000 years (Smith and Sandwell, 2006). In addition, the creeping segment also acted as a natural barrier that prevented the southwestward rupture of the 1906 Mw 7.9 San Francisco earthquake and the northeastward rupture of the 1857 Mw 7.9 Fort Tejon earthquake (Smith and Sandwell, 2006). Nevertheless, seismic hazard risk still persists along the creeping segment, as evidenced by the 2004 Mw 6.0 Parkfield earthquake (Fletcher et al., 2006) and the potential for future ruptures with magnitude up to Mw 6.5 (Maurer and Johnson, 2014). These findings

* Corresponding author.
E-mail address: tongping@ntu.edu.sg (P. Tong).

https://doi.org/10.1016/j.epsl.2026.120223
Received 8 March 2026; Received in revised form 27 May 2026; Accepted 2 July 2026
Available online 13 July 2026

underscore the need to investigate fault creep for improved assessments of earthquake potential and seismic risk.

Mechanisms contributing to the central SAF creep have been extensively studied, including frictionally weak fault gouge materials (Lockner et al., 2011; Moore and Rymer, 2007), elevated fluid pressure within the fault zone (Becken et al., 2011; Fulton and Saffer, 2009), and pressure solution creep (Gratier et al., 2011). Fluids are widely recognized as an important factor influencing fault creep, yet their specific contributions to the central SAF creep remain debated. Geophysical observations, including seismic tomography (Zeng et al., 2016) and magnetotelluric inversion (Becken et al., 2011; Bedrosian et al., 2004), reveal abundant crustal fluids beneath the creeping segment, potentially sourced from metamorphic dehydration of the Franciscan Complex and Great Valley Sequence (Berry, 1973) and/or deep mantle sources (Becken et al., 2011). Notably, fluid pressure in the Varian well, 1.4 km from the creeping segment, reaches ~ 12 MPa above hydrostatic at 1.5 km depth (Johnson and McEvilly, 1995). According to the rate- and state-dependent friction constitutive model (Dieterich, 1992), steady shear stress is expressed as $\tau_{ss} = \mu(\sigma_n - p)$, where μ denotes the effective friction coefficient, σ_n the normal stress acting on the fault plane, and p the pore pressure. Some studies suggest that fluids decrease the effective normal stress $\sigma_e = \sigma_n - p$ by elevating pore pressure p, thereby weakening the fault and promoting creep (Fulton and Saffer, 2009; Khoshmanesh and Shirzaei, 2018; Kodaira et al., 2004).

However, findings from the San Andreas Fault Observatory at Depth (SAFOD) project challenge the role of elevated pore pressure in fault creep (Zoback et al., 2010). Significantly elevated pore pressures are not observed within the fault zone during drilling at ~ 3 km depth. Instead, Lockner et al. (2011) report that the fault gouge matrix contains 60 – 65% saponite, a trioctahedral smectite clay with extremely low frictional strength ($\mu \approx 0.05$). This mineral alone is sufficient to explain the weak fault strength and creep above $\sim$3 km depth. Nevertheless, the potential role of elevated pore pressure at greater depths, where saponite becomes chemically unstable, cannot be fully ruled out (Lockner et al., 2011). Additionally, SAFOD samples reveal talc-bearing serpentinite, a frictionally weak mineral that may contribute to fault creep (Moore and Lockner, 2011; Moore and Rymer, 2007). Since talc remains stable up to ~ 800°C (Evans and Guggenheim, 1988), this mineral is proposed as the primary facilitator of creep at greater depths (Moore and Rymer, 2007).

To address the long-standing debate on the role of fluids in fault creep along the central SAF, we apply adjoint-state traveltime tomography (Chen et al., 2025a; Chen et al., 2025b; Tong, 2021) to image crustal velocity heterogeneity and azimuthal anisotropy across California (Fig. 1). The adoption of a broad study region ensures adequate data coverage within the target region near the central SAF. Seismic velocity and anisotropy are intrinsic rock properties that describe the seismic wave propagation speed and its directional dependence (Long and

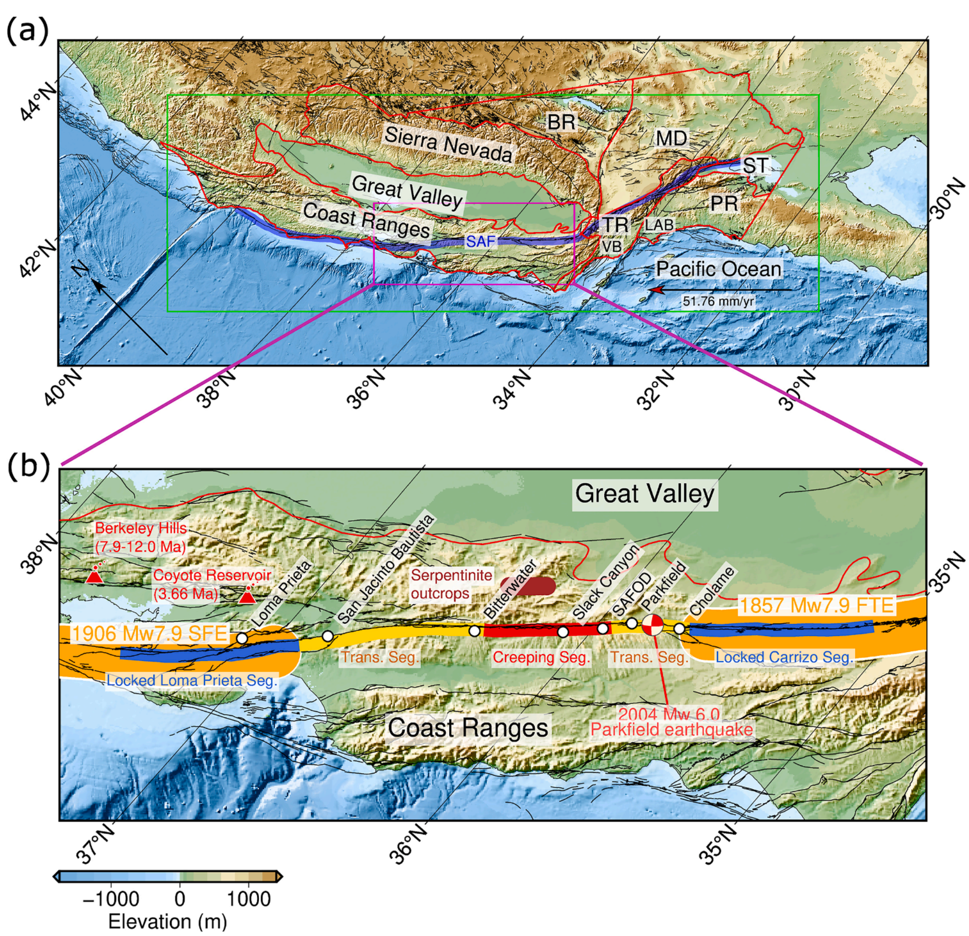

Fig. 1. Tectonic setting of the study region. (a) The computational domain (green box) with major tectonic features labeled. Red curves indicate the boundaries of these features, and the purple box outlines the central SAF study region. **(b)** Enlarged view of the central SAF. Black lines denote faults and lineaments. Thick blue, yellow, and red lines indicate the locked, transition, and creeping segments, respectively. Orange areas indicate the rupture zones of the 1906 Mw 7.9 San Francisco earthquake and the 1857 Mw 7.9 Fort Tejon earthquake. Red triangles denote the volcanic rocks near Berkeley Hills (7.9 – 12.0 Ma) and Coyote Reservoir (3.66 ± 0.01 Ma). Serpentinite outcrops are denoted by the brown zone, modified from Klein et al. (2022). BR: Basin and Range; FTE: Fort Tejon earthquake; LAB: Los Angeles Basin; MD: Mojave Desert; PR: Peninsular Ranges; SAF: San Andreas Fault; SFE: San Francisco earthquake; ST: Salton Trough; TR: Transverse Ranges; VB: Ventura Basin.

Becker, 2010). Reduced seismic velocity may indicate the presence of fluids (Smith et al., 2003), and anisotropy may reflect local stress regimes and fault zone structures in the shallow crust (Boness and Zoback, 2006). Thus, accurate velocity and anisotropy models can provide an important perspective for revealing the mechanisms by which fluids contribute to fault creep.

Our inversion incorporates first-arrival *P* and reflected *PmP* phases. The inclusion of reliably picked *PmP* data significantly improves illumination of the middle and lower crust, thereby enhancing our ability to identify crustal fluids. Leveraging an extensive dataset spanning 1981 to 2024, we obtain high-resolution images beneath the central SAF. The resulting tomographic models provide robust evidence for crustal fluids and clarify their specific contributions to fault creep along the central SAF. These observations advance our understanding of fault creep mechanisms and may be applicable to major fault systems worldwide.

2. Data and methods

2.1. Local earthquake traveltime data filtering

We download the first *P* arrivals from January 1981 to December 2024 from the Northern California Earthquake Data Center (NCEDC, 2014) and the Southern California Earthquake Data Center (SCEDC, 2013). Then, we apply strict selection criteria to improve data reliability. First, to reduce inherent picking uncertainty, only earthquakes with magnitudes greater than 2.0 are included. Second, earthquakes deeper than 20 km and events with epicentral distances exceeding 100 km are discarded, which helps mitigate the sensitivity of first *P* arrivals to uncertainties in Moho topography and uppermost mantle velocity. A lower bound of 10 km for hypocentral distance is also used to exclude extreme cases in which earthquakes occurred very close to the stations. Because these data have very short propagation paths and small traveltimes, the effect of uncertainties in traveltime picking, source parameters, and small-scale heterogeneities may become relatively significant. Third, we perform a linear regression between hypocentral distance and traveltime. Data with deviations greater than 1.74 s (three times the standard error of the estimate) are removed (Fig. S1). In addition, earthquakes with fewer than 5 reliable picks are excluded. Finally, all remaining earthquake locations are refined using the double difference location catalogs (Hauksson et al., 2012; NCEDC, 2014; SCEDC, 2013; Waldhauser and Schaff, 2008) to minimize source uncertainties. Earthquakes absent from the double difference location catalogs are discarded. After filtering, our dataset consists of 4,034,776 first *P* arrivals from 166,783 earthquakes recorded by 2047 stations (Fig. 2a).

The *PmP* traveltimes are collected from previous studies (Chen et al., 2025a; Li et al., 2024; Wu et al., 2022), which are carefully picked using a two-step semi-automatic workflow. In the first step, we manually identify the most reliable *PmP* phases based on several strict criteria. First, we consider only waveforms that most likely contain pronounced *PmP* phases, filtered by earthquake magnitudes greater than 2.0, epicentral distances of 50 – 200 km, and focal depths shallower than 20 km (Richards-Dinger and Shearer, 1997). Second, we apply a band-pass filtering between 1.0 and 7.0 Hz, and retain only waveforms with a signal-to-noise ratio (SNR) greater than 10. Third, *PmP* amplitudes should be at least twice those of *P* phases, with both exceeding the amplitude of the intervening waveform. Finally, the waveforms should contain clear *S* and *SmS* phases near the predicted arrivals. These conditions guarantee the highest-quality *PmP* phases. In the second step, we relax some limitations, such as epicentral distance, SNR threshold, and the presence of *S* and *SmS* phases. Those waveforms similar to the high-quality waveforms are manually checked and retained, with similarity defined by cross-correlation coefficients larger than 0.7. This procedure allows us to pick *PmP* phases from waveforms of moderate quality. A linear regression is performed between hypocentral distance and *PmP* traveltime (Fig. S2). The standard error of the *PmP* traveltime residuals is 0.77 s, slightly larger than that of the *P* data, 0.58 s. This difference may arise from the inherently higher picking uncertainties of *PmP* phases. Furthermore, similar to the *P* data, earthquake locations associated with the *PmP* data are also refined using the double difference location catalogs (Hauksson et al., 2012; NCEDC, 2014; SCEDC, 2013; Waldhauser and Schaff, 2008). Finally, our dataset contains 44,694 *PmP* traveltimes from 22,100 earthquakes recorded by 611 stations (Fig. 2b), with representative examples shown in Fig. S3.

2.2. Initial model and Moho topography

The initial P-wave velocity model is derived by applying the empirical function of Brocher (2005) to a three-dimensional S-wave velocity model obtained by jointly inverting receiver functions, Rayleigh wave dispersion, and ellipticity measurements (Schmandt et al., 2015). Here, we follow the method of Shen and Ritzwoller (2016). In sedimentary regions where $V_S < 3$ km/s, V_P is scaled from V_s using

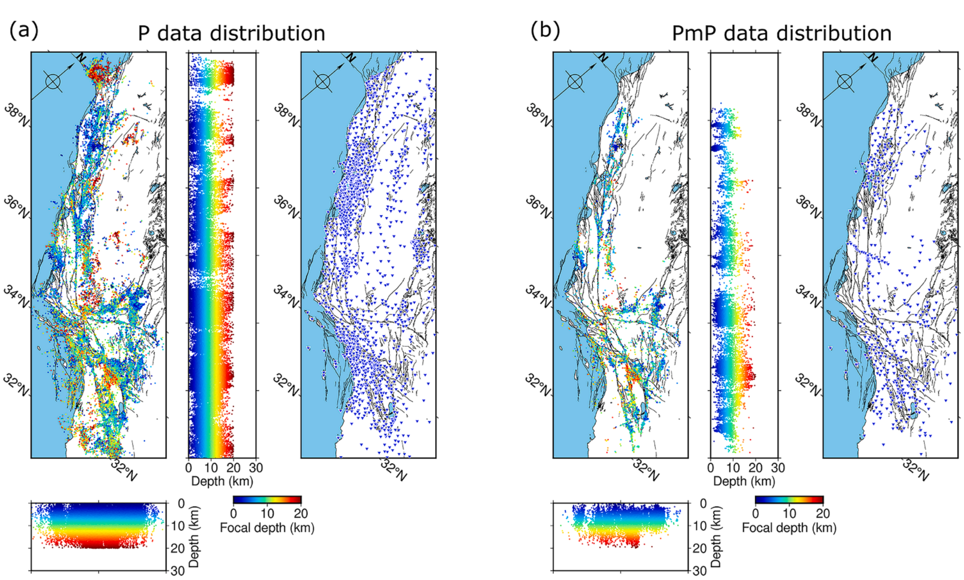

Fig. 2. Distribution of earthquakes and stations. Earthquakes, color-coded by depth, are projected onto the horizontal plane and two vertical sections. Blue inverted triangles denote seismic stations. **(a)** First arrival *P* data; **(b)** Reflected *PmP* data.

$$V_P = 0.941 + 2.095V_S - 0.821V_S^2 + 0.268V_S^3 - 0.0251V_S^4. \quad (1)$$

In the crystalline crust and uppermost mantle, a fixed V_P/V_S ratio of 1.75 is applied. The resulting Vp model is then smoothed using a Gaussian filter with standard deviations of 100 km horizontally and 2 km vertically. To further refine the initial model, we perform a preliminary inversion of *P* traveltimes on a relatively coarse inversion grid, aiming to mitigate systematic bias introduced by applying a uniform empirical function across the entire study region. This procedure yields a smoothed isotropic velocity model with a mean traveltime residual of -0.08 s, close to 0, indicating that this smoothed velocity model is suitable as an initial model for subsequent inversion (Fig. S4). Nevertheless, the mean traveltime residual varies with hypocentral distance. It is -0.18 s for data with hypocentral distances of <30 km, but becomes -0.02 s for data with hypocentral distances greater than 60 km (Fig. S5). This comparison indicates that the relatively smooth initial model cannot fully fit the observed and synthetic traveltimes over all hypocentral distance ranges, and that subsequent inversion is required to update the velocity model.

As Moho topography and lower-crustal velocity are typically coupled when inverting *PmP* traveltimes, it is essential to adopt a reliable Moho topography during the inversion. In this study, we adopt the Moho topography of Schmandt et al. (2015) (Fig. S6), which is well constrained by joint inversion of receiver functions and Rayleigh wave dispersion. This Moho topography is therefore considered reliable and is kept fixed throughout the inversion. Further refinement of the Moho depth would require additional reliable constraints, which could be explored in future work. Although the Moho model does not cover the entire study region, it fully encompasses all regions where *PmP* data are included. Areas outside the model coverage are simply filled by extrapolation, which has negligible influence on the results due to the absence of *PmP* data there.

2.3. Adjoint-state traveltime tomography

We employ adjoint-state traveltime tomography (ATT) methods to jointly invert first *P* (Chen et al., 2025b; Tong, 2021) and reflected *PmP* traveltimes (Chen et al., 2025a) for velocity heterogeneity and azimuthal anisotropy. The objective is to obtain the optimal velocity and anisotropic parameters, denoted as $(\nu^*(\boldsymbol{x}),\ \xi^*(\boldsymbol{x}), \eta^*(\boldsymbol{x}))$, that minimize the discrepancy between synthetic and observed traveltimes. We apply an iterative method to alternately minimize the following two misfit functions

$$\chi_P(\nu, \xi, \eta) = \|\boldsymbol{t}_P(\nu, \xi, \eta) - \boldsymbol{t}_P^{obs}\|^2, \quad (2)$$

$$\chi_{PmP}(\nu, \xi, \eta) = \|\boldsymbol{t}_{PmP}(\nu, \xi, \eta) - \boldsymbol{t}_{PmP}^{obs}\|^2. \quad (3)$$

Here, $\boldsymbol{t}_P(\nu, \xi, \eta)$ and $\boldsymbol{t}_{PmP}(\nu, \xi, \eta)$ denote the synthetic *P* and *PmP* traveltimes computed in the model $(\nu(\boldsymbol{x}), \xi(\boldsymbol{x}), \eta(\boldsymbol{x}))$, while $\boldsymbol{t}_P^{obs}$ and $\boldsymbol{t}_{PmP}^{obs}$ are the corresponding observations. The notation $\|\cdot\|$ represents the L_2 norm, defined as $\|\boldsymbol{t}\| = \sqrt{\sum_i t_i^2}$.

The ATT workflow comprises two primary components: forward modeling to calculate synthetic traveltimes, and inversion to iteratively update model parameters. In the forward modeling stage, the anisotropic Eikonal equation is solved using the fast sweeping method to obtain synthetic traveltimes $\boldsymbol{t}_P$ and $\boldsymbol{t}_{PmP}$ (Chen et al., 2025a). This method avoids the potential inaccuracies of conventional ray tracing techniques (e.g. bending and shooting methods) in heterogeneous and anisotropic media (Rawlinson et al., 2008). In addition, it is computationally more efficient than wave equation-based tomography methods. As a result, the forward modeling in ATT methods achieves a favorable balance between simulation accuracy and computational cost. In the inversion stage, ATT methods employ the ray-free adjoint-state method to compute sensitivity kernels. To enhance inversion stability, several postprocessing strategies are applied (Chen et al., 2025b), including multiple-grid parameterization, kernel density regularization, and step size-controlled gradient method (Text S1.1).

P traveltimes primarily constrain the upper to middle crust, whereas *PmP* traveltimes are sensitive to the entire crust, with particular sensitivity to the lower crust. To fully leverage the complementary resolving abilities of these two datasets, which differ substantially in data volume, we carefully design a two-stage inversion strategy to invert for velocity and anisotropy in the entire crust. Specifically, in the first stage, only the *P* traveltimes are inverted for 40 iterations to simultaneously update velocity, anisotropy, and source locations. In the second stage, *P* and *PmP* traveltimes are inverted alternately for 100 iterations in total, consisting of 10 inversion loops. Each loop includes 5 iterations for *PmP* data followed by 5 iterations for *P* data. Details of the inversion procedure are provided in Text S1.2. After the inversion, the standard deviations of *P* and *PmP* residuals reduce from 0.42 s and 0.75 s to 0.26 s and 0.63 s, respectively (Text S1.3). Synthetic checkerboard tests validate our inversion procedure and demonstrate that the inclusion of *PmP* data substantially improves the resolution of the middle-to-lower crust. In addition, synthetic leakage tests indicate that relatively weak leakage occurs between velocity and azimuthal anisotropy during the inversion (see Text S1.4 for details of synthetic tests).

3. Results

We obtain a three-dimensional anisotropic P-wave velocity model of the entire crust beneath California. Incorporating *PmP* data enhances illumination of the middle and lower crust down to Moho depths. Pronounced velocity heterogeneities and anisotropy anomalies are identified beneath major tectonic features, such as the Sierra Nevada, Great Valley, Coast Ranges, and southern California. Here, we focus on structures beneath the central SAF, with other regions presented and discussed in Text S2.

3.1. P-wave velocity heterogeneity

Our tomographic model reveals distinct velocity anomalies in the crust. In the upper crust above ~ 8 km depth (Figs. 3b-d, S9b-d), the most pronounced feature is the SAF that separates high-velocity zones to the southwest from low-velocity zones to the northeast. This pattern is consistent with previous tomographic studies (Eberhart-Phillips and Michael, 1993; Tong, 2021; Zeng et al., 2016). The velocity contrast across the fault exceeds 20% at 2 km depth and generally decreases to approximately 4% at 8 km depth, which reflects differences in rock type across the fault. The high-velocity region corresponds to Salinian granite rocks, while the low-velocity body represents the Great Valley Sequence which consists primarily of sediments (Wallace, 1990). In detail, the Great Valley Sequence contains two anomalies with lower velocity—one near the creeping segment at 36.3°N, 120°W, and the other near the San Francisco Bay Area at 38.0°N, 121.8°W. The peak velocity perturbations of these two anomalies reach approximately -20% at 2 km depth and decrease in magnitude to approximately -10% at 8 km depth. These features agree with models from Jiang et al. (2018) and Lin et al. (2014), and may reflect relatively thicker sedimentary deposits (Mooney and Kaban, 2010).

In the middle-to-lower crust below 10 km depth (Figs. 3e-h, S9e-h), our model reveals a prominent high-velocity anomaly of $+2$% to $+8$% beneath the Great Valley, corresponding to part of the 700-km-long and 70-km-wide Great Valley Ophiolite (GVO) (Godfrey and Klemperer, 1998). This feature aligns with previous seismic tomographic studies (Jiang et al., 2018; Lin et al., 2014) and coincides with gravity and magnetic models (Godfrey and Klemperer, 1998). In addition, our model clearly resolves four isolated low-velocity anomalies in the middle-to-lower crust along or near the central SAF. The northernmost anomaly (*L1*; 37.8°N, 122°W) underlies the Berkeley Hills volcanic center (7.9 – 12.0 Ma) (Fox et al., 1985), which is also identified by previous seismic tomographic models (Hole et al., 2000; Li et al., 2024).

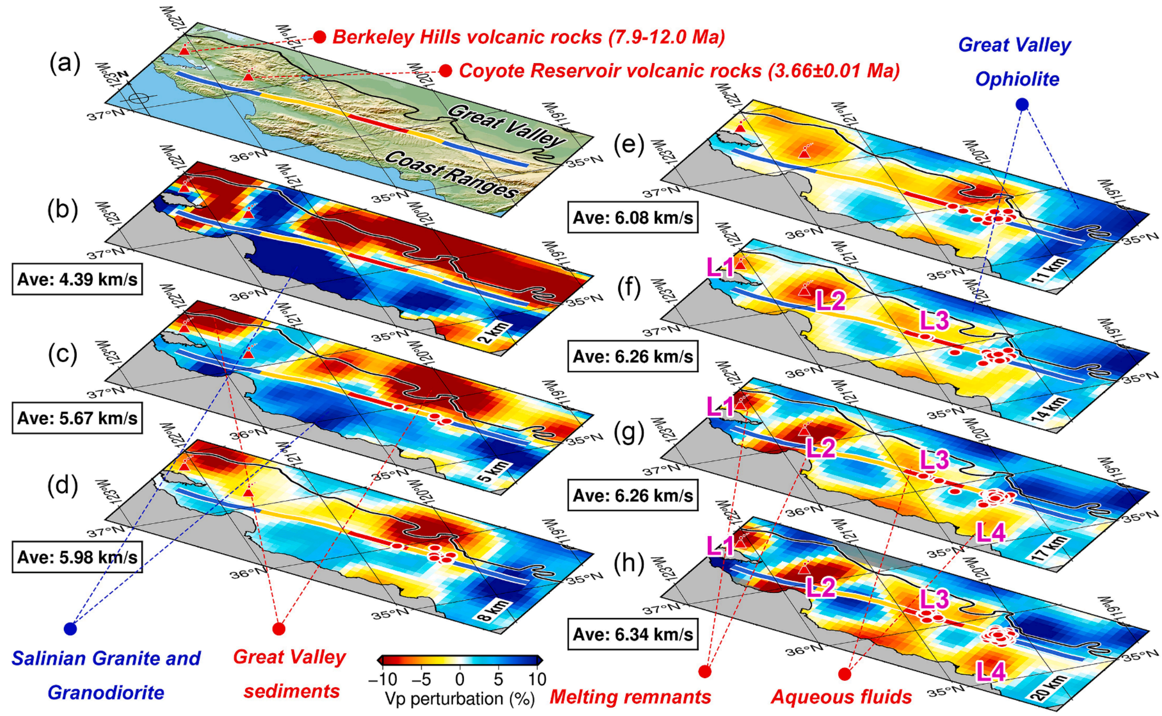

Fig. 3. Horizontal sections of P-wave velocity perturbation. (a) Topography map. Thick blue, yellow, and red lines denote the locked, transition, and creeping segments of the central San Andreas Fault. The black curve represents the boundary of the Great Valley. **(b-h)** Horizontal profiles of P-wave velocity perturbation relative to the horizontal average at different depths. Red circles mark tremor events located within 2 km of the section. Prominent features are labeled.

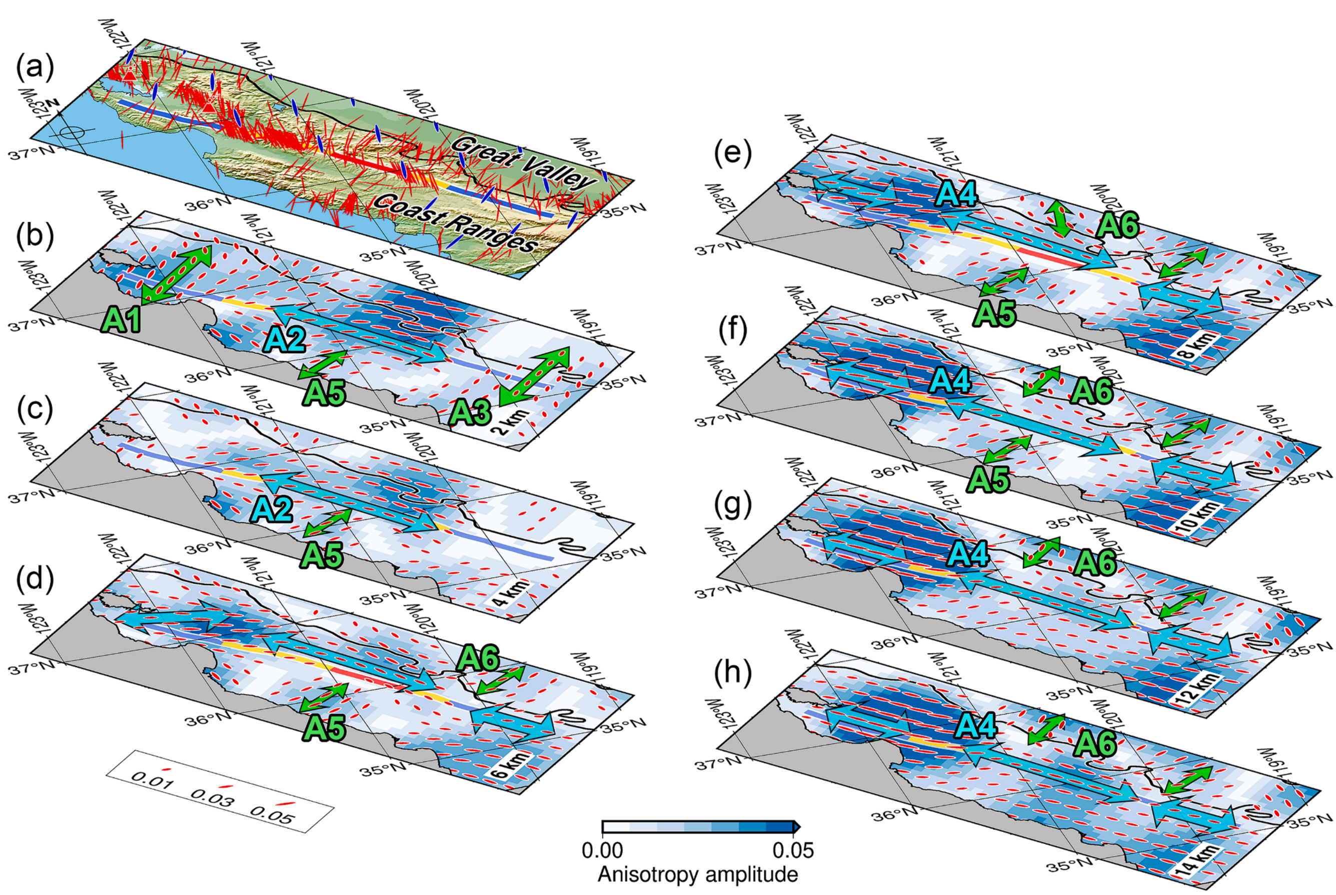

Fig. 4. Horizontal sections of P-wave azimuthal anisotropy and stress map. (a) Stress map. Red lines align with S_{Hmax} directions from the World Stress Map Database Release 2025 (Heidbach et al., 2025). Blue lines indicate the smoothed S_{Hmax} directions from the Smoothed Global Stress Maps (Heidbach and Ziegler, 2018). **(b-h)** Fast velocity directions at different depths (red bars). Labeled arrows highlight general alignment patterns of fast velocity directions.

This anomaly extends from 14 km to at least 20 km depth, with peak Vp perturbations ranging from −12% to −6%. The second anomaly (*L2*; 37.2°N, 121.5°W) lies beneath the Coyote Reservoir volcanic center (3.66 ± 0.01 Ma) (Fox et al., 1985). It also extends from 14 km to at least 20 km depth, with peak Vp perturbations ranging from −12% to −8%. This anomaly appears faintly in the Vp model of Guo et al. (2025) but is sharply imaged here due to the enhanced middle-to-lower crustal resolution by *PmP* data. The third anomaly (*L3*; 36.5°N, 120.8°W) is located beneath the transition and creeping segments. This anomaly extends from 14 km to at least 20 km depth, with peak perturbations ranging from −6% to −4%. It coincides with a ∼ 3.5 km/s low Vs anomaly at 20 km in the ambient noise tomography model of Lippoldt et al. (2017) (profile b), but is poorly resolved in the Vp model of Zeng et al. (2016) due to sparse lower-crustal low-frequency earthquakes in that region. The southernmost anomaly (*L4;* 35.5°N, 120.5°W), west of the Carrizo segment, extends from 17 km to at least 20 km depth, with peak perturbations ranging from −6% to −4%. This anomaly aligns with a ∼ 3.5 km/s low Vs anomaly at 20–25 km in the model of Lippoldt et al. (2017) (profile d). Notably, these four low-velocity anomalies are largely revealed by the *PmP* data, consistent with the checkerboard tests showing limited lower-crustal resolution using only *P* data (Text S1.4 and Fig. S21).

3.2. P-wave azimuthal anisotropy

Our model shows distinct patterns of azimuthal anisotropy in the shallow and middle crust. In the shallow crust (Fig. 4b), fast velocity directions (FVDs) along the central SAF vary significantly. NE-SW FVDs, perpendicular to the fault strike, dominate in the locked Loma Prieta (*A1*; 37.5°N, 122°W) and Carrizo segments (*A3*; 35.2°N, 120°W), with anisotropy amplitudes of approximately 0.04 and 0.02, respectively. In contrast, NW-SE FVDs, parallel to the fault strike, are imaged along the intervening transition and creeping segments (*A2*), with anisotropy amplitudes ranging from 0.02 to 0.04. This along-strike variation diminishes rapidly with depth (compare Fig. 4b with 4d). In the middle crust, FVDs along the central SAF are uniformly oriented NW-SE, parallel to the fault strike (Fig. 4d-h, *A4*). The anisotropy amplitude reaches up to 0.08 near the Loma Prieta segment but decreases to 0.01–0.03 toward the south. Additionally, two localized regions of fault-normal NE-SW FVDs (*A5* and *A6*) emerge adjacent to the central SAF, with anisotropy amplitudes of approximately 0.02. One anomaly appears west of the creeping segment down to 10 km depth (Fig. 4b-f, *A5,* 36°N, 121°W), where the FVDs align parallel to the maximum horizontal compressive stress (S_{Hmax}) from borehole measurements (Boness and Zoback, 2006) (Fig. 4a). The other anomaly lies beneath the Great Valley at depths greater than 8 km (Fig. 4e-h, *A6*), distinct from the NW-SE FVDs in the adjacent Coast Ranges.

4. Discussion

4.1. Mechanism of fluid-facilitated fault creep

The inclusion of *PmP* data enables the identification of four low-velocity anomalies (*L1-L4*) in the middle-to-lower crust, providing new insights into fluid infiltration beneath the central SAF. The two northern anomalies (*L1* and *L2*), located beneath the Berkeley Hills volcanic center (7.9 − 12.0 Ma) (Fox et al., 1985) and the Coyote Reservoir volcanic center (3.66 ± 0.01 Ma) (Fox et al., 1985; Nakata, 1981), are plausibly interpreted as melting remnants in the middle-to-lower crust. Further south, the low-velocity anomalies (*L3* and *L4*) exhibit low electrical resistivity of ∼ 10 Ωm in magnetotelluric inversions (Becken et al., 2011), indicating the presence of fluids. In contrast to *L1* and *L2*, there is no compelling evidence of historical volcanism in the regions of *L3* and *L4* (Fox et al., 1985). Furthermore, the temperature at 20 km depth near Parkfield, estimated to be ∼ 500°C based on surface heat flow modeling (Sass et al., 1997), is insufficient for partial melting (Becken et al., 2011). Thus, we infer that *L3* and *L4* likely represent aqueous fluids rather than melts. These aqueous fluids may originate from metamorphic dehydration of the Franciscan Complex in the crust (Berry, 1973) and/or from the uppermost mantle due to ongoing dehydration of serpentinized mantle wedge material (Becken et al., 2011; Fulton and Saffer, 2009).

Fluids can elevate pore pressure and facilitate fault creep by reducing effective normal stress (Becken et al., 2011; Fulton and Saffer, 2009; Zeng et al., 2016). However, the SAFOD project did not observe significantly elevated pore pressure at ∼ 3 km depth (Zoback et al., 2010), casting doubt on the role of fluids in creep (Lockner et al., 2011; Moore and Rymer, 2007). To address this issue, we attribute Vp reduction to pore fluids and estimate average crustal porosity along the central SAF using Gassmann fluid substitution modeling (Smith et al., 2003). See Text S3 for details. Porosity varies substantially along strike, from 1% to 10%, with two pronounced peaks of ∼ 10% in the locked Loma Prieta segment and ∼ 8% near the creeping segment (Fig. 5a). The porosity range is consistent with 2% − 15% estimates from magnetotelluric inversions (Bedrosian et al., 2004). The two peak porosity zones correspond to melt remnants of *L2* beneath the locked Loma Prieta segment and aqueous fluids of *L3* beneath the creeping segment, respectively. It should be noted that porosity may be overestimated because the effect of fluid-saturated crack systems is not taken into account. However, accurately correcting for the contribution of cracks to porosity estimates is challenging, because the 3D distribution of crack density and the degree of fluid saturation are not well constrained. Our rough evaluation suggests that this overestimation does not exceed 3.75% in the upper crust and is much smaller in the middle and lower crust due to pervasive crack closure under increasing confining pressure. Therefore, this uncertainty may not significantly alter the overall pattern of the estimated porosity curve (see Text S3.4 for detailed discussion).

Fluids associated with *L2* and *L3* are likely to ascend into the shallow fault zone through the fault plane, given that the SAF extends down to the lower crust and even cuts through the entire crust (Henstock et al., 1997; Parsons and Hart, 1999; Zhu, 2000). This inference is supported by magnetotelluric inversions, which reveal vertical low electrical resistivity channels (∼ 10 Ωm) beneath the Loma Prieta and the creeping segment, extending from the surface to depths exceeding 10 km (Bedrosian et al., 2004; Merzer and Klemperer, 1997). These channels imply pathways for fluid migration from the lower crust or deeper sources. In addition, elevated $^3He/^4He$ ratios (0.12 − 4.0 Ra, Ra = 1.4 × 10^{-6}, the atmospheric $^3He/^4He$ ratio) along the SAF indicate mantle He contributions of 1% − 50% (Kennedy et al., 1997) (Fig. S27), further supporting deep fluid sources.

Along the locked Loma Prieta segment and the creeping segment, both melts and aqueous fluids can reduce effective normal stress by elevating pore pressure. However, despite similarly high porosity levels, the Loma Prieta segment associated with partial melting remains locked, in contrast with the creeping segment which is related to aqueous fluids and exhibits relatively high creep rates (Jolivet et al., 2015; Titus et al., 2006) (Fig. 5). This discrepancy suggests that elevated pore pressure may not be the primary driver of fault creep along the central SAF. This interpretation is consistent with SAFOD findings, which ascribe fault creep above ∼ 3 km depth predominantly to frictionally weak materials such as saponite and talc-bearing serpentinite (Lockner et al., 2011; Moore and Rymer, 2007). Nevertheless, it is premature to rule out the role of fluids in promoting creep. Our study shows that the creep rate and porosity along the transition and creeping segments are highly correlated, with a correlation coefficient of 0.99 (Fig. 5a, 100 − 275 km from San Juan Bautista to Cholame). This strong correlation suggests that fluids indeed contribute to fault creep, though not via elevated pore pressure as commonly assumed (Fulton and Saffer, 2009; Khoshmanesh and Shirzaei, 2018; Kodaira et al., 2004).

The key difference between the two fluid reservoirs lies in their temperature and composition. Near the creeping segment, surface heat

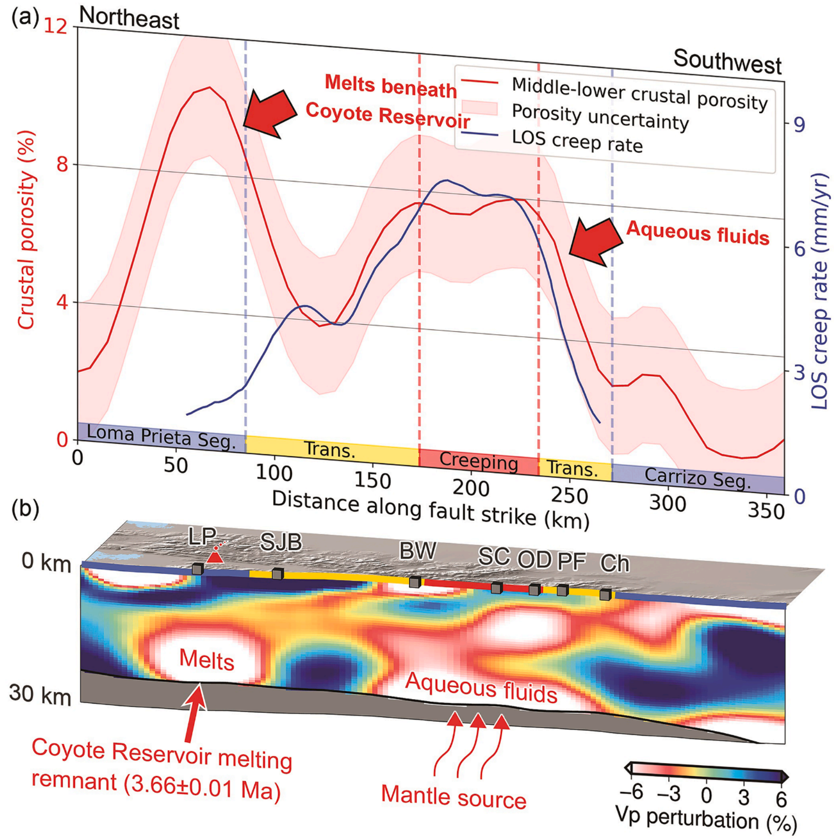

Fig. 5. Relationship between crustal fluids and creep rates. (a) The red curve shows the averaged crustal porosity, with the shaded area representing the uncertainty. The blue curve denotes the smoothed Interferometric Synthetic Aperture Radar-derived (InSAR) line-of-sight (LOS) creep rate (Jolivet et al., 2015). An InSAR LOS creep rate of 6–7 mm/year corresponds to 25–30 mm/year of plate motion parallel to the fault (Jolivet et al., 2015). **(b)** Vertical profile of velocity perturbation along the central San Andreas Fault. Perturbations are shown relative to the 1D averaged model (Fig. S29). The black curve represents the Moho interface.

flow modeling (Sass et al., 1997) estimates temperatures of $\sim 250-500^{\circ}$C at depths of $10-20$ km. This range favors the stable existence of serpentinite and talc (Evans and Guggenheim, 1988), both of which are commonly linked with fault creep (Bürgmann, 2018; Moore and Rymer, 2007). The presence of serpentinite is supported by outcrops near the creeping segment (Rymer, 1982) (Fig. 1) and SAFOD samples at ~ 3 km depth (Moore and Rymer, 2007). Additionally, talc forms along vein walls, cracks, and foliation planes within sheared serpentinite at ~ 3 km depth through metasomatic reactions with silica-rich hydrothermal fluids:

$$\text{Serpentinite} + 2SiO_2 \rightarrow \text{Talc} + H_2O.$$

With increasing depth, faster reaction rates and greater amounts of dissolved silica, due to higher temperature, will enhance metasomatic reactions. Therefore, it is reasonable to infer that serpentinite and talc persist at greater depths near the creeping segment (Moore and Rymer, 2007). As a frictionally weak material, talc-bearing serpentinite may account for fault creep in the crust (Moore and Rymer, 2007). Laboratory experiments report that higher talc content in serpentinite yields a lower coefficient of friction (Moore and Lockner, 2011). Notably, even $\sim$ 2% talc content in serpentinite can reduce the coefficient of friction from ~ 0.60 to ~ 0.25 in some cases (Moore and Lockner, 2011).

We infer that fluids facilitate the central SAF creep primarily by promoting talc formation rather than by elevating pore pressure. Increased aqueous fluid volume promotes greater dissolution of silica—a key reactant in the metasomatic reaction—yielding greater talc production. Thus, near the creeping segment, abundant crustal aqueous fluids migrate upward along the fault plane, facilitating the formation of talc within the fault gouge. The resulting talc-bearing serpentinite, being frictionally weak, reduces fault strength and promotes fault creep. By contrast, fluids beneath the Loma Prieta segment possibly correspond to melt remnants beneath the Coyote Reservoir volcanic center (3.66 ± 0.01 Ma). Temperatures required for partial melting in the lower crust can exceed 800°C (Li et al., 2024). Under such conditions, frictionally weak materials such as talc-bearing serpentinite are unlikely to persist. In addition, the lack of aqueous fluids also inhibits the formation of serpentinite and talc. Consequently, despite the potential for elevated pore pressure, the Loma Prieta segment remains locked due to the absence of frictionally weak materials. This comparison indicates that fluids promote the central SAF creep primarily by facilitating the formation of frictionally weak minerals rather than by elevating pore pressure.

4.2. Implications of anisotropic variations along the central SAF

Fault properties are also linked with seismic anisotropy. In the shallow crust (< 5 km) of the central SAF, anisotropy is primarily controlled by stress and fault structures (Boness and Zoback, 2006). The maximum horizontal compressive stress (S_{Hmax}) closes microcracks perpendicular to its direction while preserving those parallel to S_{Hmax}, resulting in stress-induced anisotropy with FVDs parallel to S_{Hmax}. In addition, shear fabrics within the fault gouge and fault-parallel macroscopic fractures tend to orient FVDs parallel to the fault strike (Johnston and Christensen, 1995; Zhang and Schwartz, 1994), which is widely observed in large strike-slip fault systems (Boness and Zoback, 2006; Zhang and Schwartz, 1994) and is termed structure-induced anisotropy (Boness and Zoback, 2006).

Seismic tomographic inversion measures the volume average of anisotropy, which enables our model to capture the competition between fault-normal stress-induced and fault-parallel structure-induced anisotropies along the central SAF. In the locked Loma Prieta and Carrizo segments, fault-normal (S_{Hmax}-parallel) FVDs dominate (Fig. 4, *A1* and *A3*), reflecting stress-induced anisotropy. Conversely, fault-parallel FVDs prevail in the intervening transition and creeping segments (Fig. 4, *A2*), indicating structure-induced anisotropy. This variation in the dominant anisotropy mechanism may be explained by two primary factors. First, SAFOD drilling reveals that the fault gouge of the creeping segment consists of a matrix of magnesium-rich clay containing porphyroclasts of serpentinite and sedimentary rock (Lockner et al., 2011). The preferred orientation of foliated clay minerals within the fault gouge can reduce P-wave speed normal to the fault by $\sim 30\%$ (Johnston and Christensen, 1995), contributing to fault-parallel FVDs. X-ray diffraction analyses indicate that saponite is a key component of the fault gouge and can constitute over 60% (Lockner et al., 2011). This mineral contributes to a frictionally weak ($\mu \approx 0.15$) and velocity strengthening ($a - b > 0.0037 \pm 0.0007$) fault gouge, promoting creep behavior (Lockner et al., 2011). Thus, the fault-parallel anisotropy along the creeping segment also highlights the presence of frictionally weak minerals and their role in facilitating fault creep. Second, focal mechanism inversions and borehole breakouts (Mount and Suppe, 1987) indicate an angle of $\sim 85^\circ$ between S_{Hmax} and the fault strike near the Loma Prieta segment, higher than the $\sim 70^\circ$ angle near the creeping segment (Townend and Zoback, 2004) (Figs. 4a, S26, S28). The higher angle of $\sim 85^\circ$ may suggest enhanced fault-normal stress, favoring stress-induced anisotropy as the dominant mechanism in the Loma Prieta segment.

With increasing depth, confining pressure gradually closes microcracks, thereby diminishing microcrack-related anisotropy and making the crystallographic preferred orientation (CPO) of minerals the dominant mechanism (Crampin, 1987). Below 5 km depth, pervasive fault-parallel FVDs are imaged along the central SAF (Fig. 4, *A4*), likely attributed to the CPO of minerals (Kim and Jung, 2019; Zhang and Schwartz, 1994). Middle-crustal rocks, such as amphibole and mica, experience intense shear deformation due to the relative motion of the Pacific and North American plates, producing FVDs parallel to the plate-motion direction (i.e., parallel to the fault strike) (Almqvist and Mainprice, 2017; Kim and Jung, 2019). In addition, stress-parallel FVDs west of the SAF at $2-10$ km depth (Fig. 4, *A5*) likely arise from preferred orientations of open microcracks (Tong, 2021). These cracks persist down to 10 km depth, possibly due to fluid infiltration (Audet, 2015), as supported by the low electrical resistivity anomaly there (Becken et al., 2011). Furthermore, fault-normal FVDs within the Great Valley Ophiolite (GVO) below 8 km depth stand in contrast to fault-parallel FVDs in the Coast Ranges to the northwest (Fig. 4, *A6*). As proposed by Godfrey and Klemperer (1998), the GVO formed through spreading and was subsequently accreted to the continental margin during the Nevadan orogeny, ultimately forming the basement of the Great Valley basin. The fault-normal FVDs within the GVO possibly result from the inherited structures and fabrics with limited rotation.

5. Conclusions

By jointly inverting first arrival *P* and reflected *PmP* phases, we image crustal velocity heterogeneity and azimuthal anisotropy across California. The inclusion of *PmP* data significantly enhances the identification of fluids in the middle-to-lower crust, revealing a nearly proportional relationship between creep rate and aqueous fluid volume along the central SAF. In contrast, the Loma Prieta segment remains locked despite the potential for elevated pore pressure associated with melts. This comparison suggests that elevated pore pressure, arising from either aqueous fluids or melts, is not the primary driver of fault creep. Instead, aqueous fluids may promote fault creep primarily by facilitating the formation of frictionally weak materials, such as talc-bearing serpentinite. Our anisotropic model further indicates the presence of frictionally weak minerals in the creeping segment. However, our model explains the mechanisms of creep only for the central SAF, and its applicability beyond this fault system is uncertain. Fault creep is also observed in other fault systems worldwide, such as the North Anatolian Fault and Alto Tiberina Fault. The mechanisms that drive fault creep are multifaceted and likely arise from the combined effects of multiple factors. Further studies are required to investigate the underlying mechanisms and to evaluate the extent to which our interpretation can be generalized to other fault systems.

CRediT authorship contribution statement

Jing Chen: Conceptualization, Data curation, Formal analysis, Investigation, Methodology, Project administration, Resources, Software, Validation, Visualization, Writing – original draft, Writing – review & editing. **Tianjue Li:** Data curation, Methodology, Validation, Writing – review & editing. **Xiao Xiao:** Formal analysis, Investigation, Writing – review & editing. **Shucheng Wu:** Data curation, Investigation, Writing – review & editing. **Yiming Bai:** Formal analysis, Visualization, Writing – review & editing. **Guoxu Chen:** Data curation, Methodology, Software, Writing – review & editing. **Bingfeng Zhang:** Formal analysis, Visualization, Writing – review & editing. **Mijian Xu:** Formal analysis, Software, Writing – review & editing. **Ping Tong:** Conceptualization, Data curation, Formal analysis, Funding acquisition, Methodology, Project administration, Resources, Supervision, Validation, Writing – review & editing.

Declaration of competing interest

The authors declare that they have no known competing financial interests or personal relationships that could have appeared to influence the work reported in this paper.

Acknowledgments

This work was supported by the Ministry of Education, Singapore, under its MOE AcRF Tier-3 Grant (MOE-MOET32021-0002 to P.T.), the Ministry of Education, Singapore, under its MOE AcRF Tier-2 Grant (MOE-T2EP20124-0003 to P.T.), and the Indonesian Endowment Fund for Education (LPDP) on behalf of the Indonesian Ministry of Higher Education, Science, and Technology and managed under the INSPIRASI Program (Grant Nos. 2924/E3/AL.04/2024 and 4809/UN.I/PK.08.00/2024 to P.T.). The authors appreciate the first-arrival P traveltime catalog provided by the Northern California Earthquake Data Center (NCEDC, 2014) and the Southern California Earthquake Data Center (SCEDC, 2013). The inversion of first P arrivals was implemented using the open-source tomographic package TomoATT (https://tomoatt.com) (Chen et al., 2025b). The computational work for this article was fully performed on resources of the National Supercomputing Centre, Singapore (https://www.nscc.sg). The authors thank Hans Thybo, Hayrullah Karabulut, and an anonymous reviewer for their constructive suggestions and valuable comments, which helped improve this article.

Supplementary materials

Supplementary material associated with this article can be found, in the online version, at doi:10.1016/j.epsl.2026.120223.

Data availability

Three-dimensional models of P-wave velocity and azimuthal anisotropy are available via https://doi.org/10.21979/N9/CD8LCR.

References

Almqvist, B.S., Mainprice, D., 2017. Seismic properties and anisotropy of the continental crust: predictions based on mineral texture and rock microstructure. Rev. Geophys. 55 (2), 367–433.

Audet, P., 2015. Layered crustal anisotropy around the San Andreas Fault near Parkfield, California. J. Geophys. Res.: Solid Earth 120 (5), 3527–3543.

Becken, M., Ritter, O., Bedrosian, P.A., Weckmann, U., 2011. Correlation between deep fluids, tremor and creep along the central San Andreas fault. Nature 480 (7375), 87–90.

Bedrosian, P., Unsworth, M., Egbert, G., Thurber, C., 2004. Geophysical images of the creeping segment of the San Andreas fault: implications for the role of crustal fluids in the earthquake process. Tectonophysics. 385 (1–4), 137–158.

Berry, F.A., 1973. High fluid potentials in California Coast Ranges and their tectonic significance. Am. Assoc. Pet. Geol. Bull. 57 (7), 1219–1249.

Boness, N.L., Zoback, M.D., 2006. Mapping stress and structurally controlled crustal shear velocity anisotropy in California. Geology. 34 (10), 825.

Bürgmann, R., 2018. The geophysics, geology and mechanics of slow fault slip. Earth. Planet. Sci. Lett. 495, 112–134.

Brocher, T.M., 2005. Empirical relations between elastic wavespeeds and density in the Earth's crust. Bull. Seismol. Soc. Am. 95 (6), 2081–2092.

Chen, G., Chen, J., Li, T., Xu, M., Zhao, Q., Tong, P., 2025a. Adjoint-state reflection traveltime tomography for velocity and interface inversion with its application in Central California near Parkfield. J. Geophys. Res.: Solid Earth 130 (1), e2024JB029918.

Chen, J., Nagaso, M., Xu, M., Tong, P., 2025b. TomoATT: an open-source package for eikonal equation-based adjoint-state traveltime tomography for seismic velocity and azimuthal anisotropy. Comput. Geosci. 204, 105995.

Crampin, S., 1987. Geological and industrial implications of extensive-dilatancy anisotropy. Nature 328 (6130), 491–496.

Dieterich, J.H., 1992. Earthquake nucleation on faults with rate-and state-dependent strength. Tectonophysics. 211 (1–4), 115–134.

Eberhart-Phillips, D., Michael, A.J., 1993. Three-dimensional velocity structure, seismicity, and fault structure in the Parkfield region, central California. J. Geophys. Res.: Solid Earth 98 (B9), 15737–15758.

Evans, B., Guggenheim, S., 1988. Talc, pyrophyllite, and related minerals. Rev. Mineral. Geochem. 19 (1), 225–294.

Fletcher, J.B., Spudich, P., Baker, L.M., 2006. Rupture propagation of the 2004 Parkfield, California, earthquake from observations at the UPSAR. Bull. Seismol. Soc. Am. 96 (4B), S129–S142.

Fox Jr, K.F., Fleck, R.J., Curtis, G.H., Meyer, C.E., 1985. Implications of the northwestwardly younger age of the volcanic rocks of west-central California. Geol. Soc. Am. Bull. 96 (5), 647.

Fulton, P.M., Saffer, D.M., 2009. Potential role of mantle-derived fluids in weakening the San Andreas Fault. J. Geophys. Res.: Solid Earth 114 (B7), B07408.

Godfrey, N.J., Klemperer, S.L., 1998. Ophiolitic basement to a forearc basin and implications for continental growth: the Coast Range/Great Valley ophiolite, California. Tectonics. 17 (4), 558–570.

Gratier, J.P., Richard, J., Renard, F., Mittempergher, S., Doan, M.L., Di Toro, G., et al., 2011. Aseismic sliding of active faults by pressure solution creep: evidence from the San Andreas Fault Observatory at depth. Geology. 39 (12), 1131–1134.

Guo, H., Taira, T.a., Nayak, A., Thurber, C., Hirakawa, E., 2025. Three-dimensional seismic velocity models for the San Francisco Bay region, California from joint body-wave and surface-wave tomography validated by waveform simulation. J. Geophys. Res.: Solid Earth 130 (6), e2025JB031377.

Hauksson, E., Yang, W., Shearer, P.M., 2012. Waveform relocated earthquake catalog for Southern California (1981 to June 2011). Bull. Seismol. Soc. Am. 102 (5), 2239–2244.

Heidbach, O., Rajabi, M., Di Giacomo, D., Harris, J., Lammers, S., Morawietz, S., et al., 2025. World Stress Map database Release 2025. GFZ Data Services. https://doi.org/10.5880/WSM.2025.001. *Dataset.*

Heidbach, O., Ziegler, M., 2018. Smoothed global stress maps based on the World Stress Maps database release 2016. GFZ Data Services. https://doi.org/10.5880/WSM.2018.002. *Dataset.*

Henstock, T.J., Levander, A., Hole, J.A., 1997. Deformation in the lower crust of the San Andreas fault system in northern California. Science 278 (5338), 650–653.

Hole, J.A., Brocher, T., Klemperer, S., Parsons, T., Benz, H., Furlong, K., 2000. Three-dimensional seismic velocity structure of the San Francisco Bay area. J. Geophys. Res.: Solid Earth 105 (B6), 13859–13874.

Jiang, C., Schmandt, B., Hansen, S.M., Dougherty, S.L., Clayton, R.W., Farrell, J., Lin, F.-C., 2018. Rayleigh and S wave tomography constraints on subduction termination and lithospheric foundering in central California. Earth. Planet. Sci. Lett. 488, 14–26.

Johnson, P., McEvilly, T., 1995. Parkfield seismicity: fluid-driven? J. Geophys. Res.: Solid Earth 100 (B7), 12937–12950.

Johnston, J.E., Christensen, N.I., 1995. Seismic anisotropy of shales. J. Geophys. Res.: Solid Earth 100 (B4), 5991–6003.

Jolivet, R., Simons, M., Agram, P., Duputel, Z., Shen, Z.K., 2015. Aseismic slip and seismogenic coupling along the central San Andreas Fault. Geophys. Res. Lett. 42 (2), 297–306.

Kennedy, B., Kharaka, Y., Evans, W.C., Ellwood, A., DePaolo, D., Thordsen, J., et al., 1997. Mantle fluids in the San Andreas fault system, California. Science 278 (5341), 1278–1281.

Khoshmanesh, M., Shirzaei, M., 2018. Episodic creep events on the San Andreas Fault caused by pore pressure variations. Nat. Geosci. 11 (8), 610–614.

Kim, J., Jung, H., 2019. New crystal preferred orientation of amphibole experimentally found in simple shear. Geophys. Res. Lett. 46 (22), 12996–13005.

Klein, F., Goldsby, D.L., Lin, J., Andreani, M., 2022. Carbonation of serpentinite in creeping faults of California. Geophys. Res. Lett. 49 (15), e2022GL099185.

Kodaira, S., Iidaka, T., Kato, A., Park, J.-O., Iwasaki, T., Kaneda, Y., 2004. High pore fluid pressure may cause silent slip in the Nankai Trough. Science 304 (5675), 1295–1298.

Li, T., Wu, S., Tong, P., 2024. Multilevel transcrustal magmatic system beneath the Geysers-Clear Lake area. Proc. Natl. Acad. Sci. USA 121 (12), e2317809121.

Lin, F.-C., Tsai, V.C., Schmandt, B., 2014. 3-D crustal structure of the western United States: application of Rayleigh-wave ellipticity extracted from noise cross-correlations. Geophys. J. Int. 198 (2), 656–670.

Lippoldt, R., Porritt, R.W., Sammis, C.G., 2017. Relating seismicity to the velocity structure of the San Andreas Fault near Parkfield, CA. Geophys. J. Int. 209 (3), 1740–1745.

Lockner, D.A., Morrow, C., Moore, D., Hickman, S., 2011. Low strength of deep San Andreas fault gouge from SAFOD core. Nature 472 (7341), 82–85.

Long, M.D., Becker, T.W., 2010. Mantle dynamics and seismic anisotropy. Earth. Planet. Sci. Lett. 297 (3–4), 341–354.

Maurer, J., Johnson, K., 2014. Fault coupling and potential for earthquakes on the creeping section of the central San Andreas Fault. J. Geophys. Res.: Solid Earth 119 (5), 4414–4428.

McLaskey, G.C., Glaser, S.D., 2011. Micromechanics of asperity rupture during laboratory stick slip experiments. Geophys. Res. Lett. 38 (12).

Merzer, M., Klemperer, S.L., 1997. Modeling low-frequency magnetic-field precursors to the Loma Prieta earthquake with a precursory increase in fault-zone conductivity. Pure Appl. Geophys. 150 (2), 217–248.

Mooney, W.D., Kaban, M.K., 2010. The North American upper mantle: density, composition, and evolution. J. Geophys. Res.: Solid Earth 115 (B12), B12424.

Moore, D.E., Lockner, D.A., 2011. Frictional strengths of talc-serpentine and talc-quartz mixtures. J. Geophys. Res.: Solid Earth 116 (B1), B01403.

Moore, D.E., Rymer, M.J., 2007. Talc-bearing serpentinite and the creeping section of the San Andreas fault. Nature 448 (7155), 795–797.

Mount, V.S., Suppe, J., 1987. State of stress near the San Andreas fault: implications for wrench tectonics. Geology. 15 (12), 1143.

Nakata, J.K., 1981. Distribution and petrology of the Anderson-Coyote Reservoir volcanic rocks. U.S. Geological Survey Open-File Report 80-1256, x, 130 p., https://doi.org/10.3133/ofr801256.

NCEDC, 2014. Northern California Earthquake Data Center. UC Berkeley Seismological Laboratory. https://doi.org/10.7932/NCEDC. *Dataset.*

Parsons, T., Hart, P.E., 1999. Dipping San Andreas and Hayward faults revealed beneath San Francisco Bay, California. Geology. 27 (9), 839.

Rawlinson, N., Hauser, J., Sambridge, M., 2008. Seismic ray tracing and wavefront tracking in laterally heterogeneous media. Adv. Geophys. 49, 203–273.

Richards-Dinger, K.B., Shearer, P.M., 1997. Estimating crustal thickness in southern California by stacking PmP arrivals. J. Geophys. Res.: Solid Earth 102 (B7), 15211–15224.

Rymer, M.J. (1982). Geologic map along a 12 kilometer segment of the San Andreas fault zone, southern Diablo Range, California. U.S. Geological Survey Open-File Report 81-1173. https://doi.org/10.3133/ofr811173.

Sass, J., Williams, C., Lachenbruch, A.H., Galanis Jr, S., Grubb, F., 1997. Thermal regime of the San Andreas fault near Parkfield, California. J. Geophys. Res.: Solid Earth 102 (B12), 27575–27585.

SCEDC. (2013). Southern California Earthquake Center. Caltech. https://doi.org/10.7909/C3WD3xH1. *Dataset.*

Schmandt, B., Lin, F.C., Karlstrom, K.E., 2015. Distinct crustal isostasy trends east and west of the Rocky Mountain Front. Geophys. Res. Lett. 42 (23), 10,290-10,298.

Shen, W., Ritzwoller, M.H., 2016. Crustal and uppermost mantle structure beneath the United States. J. Geophys. Res.: Solid Earth 121 (6), 4306–4342.

Smith, T.M., Sondergeld, C.H., Rai, C.S., 2003. Gassmann fluid substitutions: a tutorial. Geophysics 68 (2), 430–440.

Smith, B.R., Sandwell, D.T., 2006. A model of the earthquake cycle along the San Andreas Fault System for the past 1000 years. J. Geophys. Res.: Solid Earth 111 (B1).

Steinbrugge, K.V., Zacher, E.G., Tocher, D., Whitten, C.A., Claire, C.N., 1960. Creep on the San Andreas fault. Bull. Seismol. Soc. Am. 50 (3), 389–415.

Titus, S.J., DeMets, C., Tikoff, B., 2006. Thirty-five-year creep rates for the creeping segment of the San Andreas Fault and the effects of the 2004 Parkfield earthquake: constraints from alignment arrays, continuous global positioning system, and creepmeters. Bull. Seismol. Soc. Am. 96 (4B), S250–S268.

Tong, P., 2021. Adjoint-state traveltime tomography for azimuthally anisotropic media and insight into the crustal structure of central California near Parkfield. J. Geophys. Res.: Solid Earth 126 (10), e2021JB022365.

Townend, J., Zoback, M.D., 2004. Regional tectonic stress near the San Andreas fault in central and southern California. Geophys. Res. Lett. 31 (15), L15S11.

Uchida, N., Bürgmann, R., 2019. Repeating earthquakes. Annu Rev. Earth. Planet. Sci. 47 (1), 305–332.

Waldhauser, F., Schaff, D.P., 2008. Large-scale relocation of two decades of Northern California seismicity using cross-correlation and double-difference methods. J. Geophys. Res.: Solid Earth 113 (B8).

Wallace, R.E. (Ed.), 1990. The San Andreas Fault System, California. U.S. Geological Survey Professional Paper 1515, 283 p., https://doi.org/10.3133/pp1515.

Wu, S., Li, T., Wang, D., Tong, P., 2022. Lower crust structures and dynamics of southern California revealed by first P and PmP traveltime data. Tectonophysics. 830, 229328.

Zeng, X., Thurber, C.H., Shelly, D.R., Harrington, R.M., Cochran, E.S., Bennington, N.L., et al., 2016. 3-D P- and S-wave velocity structure and low-frequency earthquake locations in the Parkfield, California region. Geophys. J. Int. 206 (3), 1574–1585.

Zhang, Z., Schwartz, S.Y., 1994. Seismic anisotropy in the shallow crust of the Loma Prieta segment of the San Andreas Fault System. J. Geophys. Res.: Solid Earth 99 (B5), 9651–9661.
Zhu, L., 2000. Crustal structure across the San Andreas Fault, southern California from teleseismic converted waves. Earth. Planet. Sci. Lett. 179 (1), 183–190.
Zoback, M., Hickman, S., Ellsworth, W., 2010. Scientific drilling into the San Andreas fault zone. Eos, Trans. Am. Geophys. Union 91 (22), 197–199.